

This article has been published in: *Microscopy and Microanalysis*. 2016  
Oct;22(5):1034-1046.

**Title:** Zinc-containing restorations create amorphous biogenic apatite at the carious dentin-interface: a XRD crystal-lattice analysis.

**Brief title:** XRD analysis of thermocycled restorations.

**Authors:** Manuel Toledano<sup>1\*</sup>, Fátima S. Aguilera<sup>1</sup>, Modesto T. López-López<sup>2</sup>, Estrella Osorio<sup>1</sup>, Manuel Toledano-Osorio<sup>1</sup>, Raquel Osorio<sup>1</sup>.

**Institution:** <sup>1</sup>University of Granada, Faculty of Dentistry, Dental Materials Section.

**Address:** <sup>1</sup>University of Granada, Faculty of Dentistry, Dental Materials Section

Colegio Máximo de Cartuja s/n

18071 – Granada - Spain.

<sup>2</sup>University of Granada, Faculty of Science, Applied Physics Department

Fuente Nueva s/n

18071 – Granada - Spain.

\*Corresponding author: Prof. Manuel Toledano

University of Granada, Faculty of Dentistry

Dental Materials Section

Colegio Máximo de Cartuja s/n

18071 – Granada - Spain.

Tel.: +34-958243788

Fax: +34-958240809

Email: [toledano@ugr.es](mailto:toledano@ugr.es)

## **Abstract**

The aim of this research was to assess the ability of amalgam restorations to induce amorphous mineral precipitation at the caries-affected-dentin substrate. Sound and caries-affected dentin surfaces were subjected to both Zn-free and Zn-containing dental amalgam restorations. Specimens were submitted to thermocycling (100,000cy/5 °C-55 °C, 3 months). Dentin surfaces were studied by atomic force microscopy (AFM/nano-roughness), X-ray diffraction ( $\mu$ XRD<sup>2</sup>), field emission electron microscopy (FESEM) and energy-dispersive analysis (EDX), for physical and morphological surface characterization. Zn-containing amalgam placement reduced crystallinity, crystallite size and grain size of calcium phosphate crystallites at the dentin surface. Both microstrain and nanoroughness augmented in caries-affected dentin restored with Zn-containing amalgams. Caries-affected dentin showed the shortest mineral crystallites (11.04 nm), when Zn-containing amalgams were used for restorations, probably leading to a decrease of mechanical properties which might favor crack propagation and deformation. Sound dentin restored with Zn-free amalgams exhibited a substantial increase in length of grain particles (12.44 nm) embedded into dentin crystallites. Zn-containing amalgam placement creates dentin mineralization and the resultant mineral was, utterly, amorphous in nature. Amorphous calcium phosphate will provide a local ion-rich environment which is considered favorable for *in situ* generation of prenucleation clusters, succeeding further dentin remineralization.

## **Key words**

dentin, amalgam, zinc, mineral, XRD, AFM.

## INTRODUCTION

Dentin is a complex hydrated fiber-reinforced biological composite that serves as an elastic support for enamel (Vaseenon, 2011). Its structure is composed of 70 % inorganic hydroxyapatite (HAp) crystal by weight or 50% HAp crystal by volume, in the form of a sub-micrometer to nanometer-sized carbonate rich, calcium deficient apatite crystallites ( $\sim 5 \times 30 \times 100$  nm), dispersed between parallel, micrometer-sized, hypermineralized, collagen-poor, hollow cylinders, dentinal tubules, containing peritubular dentin (Marshall, 1997). Intertubular dentin lies between the dentinal tubules and has a lower mineral content compared to peritubular dentin. The mineral content in dentin consists of crystallites whose size is approximately of the order of magnitude less compared to enamel crystallites. The c-axis of crystallites in dentin, as in other mature hard tissues, is distributed along extended collagen fibers. The size and texture of crystallites depend on their location in the tooth, kind of the tooth and maturity of the tissue (Gawda et al., 2004). The mineral phases of dentin can be described as calcium HAp with the ideal formula of  $\text{Ca}_{10}(\text{PO}_4)_6(\text{OH})_2$  (Kay et al., 1964). The biological HAp is not pure, containing carbonate-containing apatites and some other elements as magnesium (Mg), phosphate ( $\text{PO}_4$ ), chloride (Cl), fluoride (F), sodium (Na), carbonate ( $\text{CO}_3$ ), among others (Vaseenon, 2011). The biological apatites have a formula of  $(\text{Ca}, \text{Mg}, \text{Na}, \text{X})_{10}(\text{PO}_4, \text{HPO}_4, \text{CO}_3)_6(\text{OH}, \text{Cl})_2$  and is called carbonate HAp (LeGeros, 1990). The organic matter represents 18% by weight or 18% by volume, which is largely a felt-work of type I collagen (90%) and noncollagenous proteins (10%) such as dentin matrix protein and dentin phosphoproteins. Approximately, 25 vol% of the dentin content is fluid. The changes in the surface structure of dentin caused by caries may lead to significant impairment of the normal function of teeth, and eventually, lost of teeth (Fujisaki et al., 2012).

Dentin is subjected to an uneven stress distribution with localized stress concentrations because of the peri-intertubular dentin, micro-scale cavities. It is also exposed to unusual changes of temperature and force transfer in the tissue due to biting hard food and poor matching of the biting surfaces of teeth (Fujisaki et al., 2012; Toledano et al., 2015a). These stress concentration generate cracks that may cause the tooth to fracture. Thermal cycling is conventionally used to simulate the thermal changes that occur in the oral cavity during eating, drinking, or breathing which may stress the restorative interface. Mechanical stresses induced by differential thermal changes can directly induce fatigue propagation, fracture, and fluid flow through this restorative interface (Mazzitelli et al., 2012).

Amalgam restorations still have higher functional durability than resin composites (Moraschini et al., 2015; Sjögren & Halling, 2002). Despite aesthetic requirements, the mechanical properties, longevity and mainly the functional rehabilitation prevail as the most important criteria when choosing the restorative material (Moraschini et al., 2015; Qvist et al., 1990). Moreover, amalgam restorations reduce the possibility of secondary caries over time by forming oxides in the margin of the cavities as a result of the natural corrosion of the material. These corrosion products at the interface and further uptake of metal ions associated or not to Zn-containing amalgams might have performed as nuclei for apatite precipitation at the collagen fibers (Toledano et al., 2015b). Nevertheless, zinc has been widely used in dentistry, and it has been experimentally incorporated into several resin adhesives, reducing MMPs-mediated collagen degradation, inducing dentin remineralization at the bonded interface, and preserving the bonding efficacy over time (Toledano et al., 2013). To incorporate this doping agent within the chemical formulation of resin composites for restorations poses a future challenge.

Previously, it has been proved that Zn-containing amalgams restorations submitted to three weeks of load cycling promoted intrafibrillar mineralization, *i.e.*, functional

remineralization (Bertassoni et al., 2009), of the partially mineral-depleted in caries-affected dentin surfaces. These outcomes have provided information on structure and mechanical, morphological physical and chemical changes produced at micro and nano-scale at demineralized dentin below Zn-containing amalgams (Toledano et al., 2015c); however, additional correlation analyses of properties of the whole new surface are still needed. In this line, it is recommended to determine the grain size and lattice strain accordingly determined by measuring the deviation of line profile from perfect crystal diffraction, and so the preferred orientation of crystallites. Thereby, it is required to assess the capacity to absorb thermal shock waves and alleviate stresses, at these locations, in order to prevent crack propagation across the boundary between the two phases of dentin. Thus, it also may serve as useful biomimetic models for joining thermally dissimilar biomaterials to restore teeth form and function.

The HAp crystal structure is altered by tooth decay in the early stage of caries. As HAp-like mineral material has a hexagonal crystal structure, X-ray diffraction can be used to analyze its micro/nano-scale structure (Fujisaki et al., 2012), with particular emphasis on the lattice structure (Hanschin & Stern, 1995). Dentin structure can be affected by atomics substitutions within the crystal lattice and induce limitations in size of the well-ordered domains. It also can be influenced by the presence of strain or distortion resulting from eventual dislocation within the lattice (imperfection) and /or internal disorder (Hanschin & Stern, 1995). The mechanical properties of macroscopic dentin are strongly dependent on the alignment and orientation of the HAp crystals (Habelitz et al., 2001). The strain distribution is an important indicator of the stiffness of teeth as force bearing tissue during actual biting (Fujisaki et al., 2012). X-ray diffraction analysis can be used to perform quantitative measurements of both the crystal orientation and the lattice strain on the tooth surface (Fujisaki et al., 2012). X-ray micro-diffractography ( $\mu$ XRD<sup>2</sup>) with high resolution makes

possible to analyze a dental surface *in situ* without destruction and milling. Moreover, it has been possible to apply this non-destructive technique in carious and normal selected microzone areas (Xue et al., 2008).

In the present study, crystallinity, crystallite size, grain size, lattice strain and texture of human dentin substrata were physically evaluated. This analysis was complemented with atomic force (AFM), and field emission scanning electron microscopy (FESEM), and energy dispersive analysis (EDX). The tested null hypothesis was that there are no differences in physical and morphological characteristics of sound and caries-affected substrata after removal of Zn-free vs containing amalgam restorations.

## **MATERIAL AND METHODS**

### **Specimens preparation and thermocycling**

Nine extracted carious third molars without opposing occlusion were employed for the study. They were stored in 0.01% (w/v) thymol at 4° C for less than 1 month. Teeth were collected after written patients' informed consent (20 to 40 yr of age), under a protocol approved by the Institution Review Board (891/2014). Specimens were randomly assigned to three groups (n = 3) according to the type of amalgam to be used: with or without zinc; one group remained untreated. The inclusion criteria for carious dentin substrate were as in Toledano et al. (2016). Flat mid-coronal sound dentin, and caries affected dentin surfaces surrounded by normal dentin, were exposed using a hard tissue microtome (Accutom-50; Struers, Copenhagen, Denmark) equipped with a slow-speed, water-cooled diamond wafering saw (330-CA RS-70300, Struers, Copenhagen, Denmark). Molars were transversally sectioned (Isomet 4000, Buehler, Lake Bluff, IL, USA) at the mid-coronal portion of each tooth, to produce dentin discs (2.5 mm thick), one per tooth, and were polished through SiC abrasive papers up to 4,000-grit with a final polishing procedure performed with diamond

pastes (Buehler-MetaDi, Buehler Ltd.), through 1  $\mu\text{m}$  down to 0.25  $\mu\text{m}$ . The specimens were treated in ultrasonic bath (Model QS3, Ultrawave Ltd, Cardiff, UK) containing deionized water [pH 7.4] for 5 min at each polishing step.

Two third of teeth were restored with amalgam. Two self threading titanium retentive pins (4.4 mm length) (STP Restorative Dentsply Maillefer, Ballaigues, Switzerland) were used to retain the amalgam restorations, by using copper bands (Copper Bands, Hard. AB Dentatus, Spånga, Sweden), surrounding the prepared dentin discs. A tile of Zn-free vs Zn-containing dental amalgam was condensed on top of the disc surfaces in a layer of at least 3 mm thick. Finally, the amalgam surfaces were finished with hand instruments. The detailed composition of each amalgam is shown in Table 1. The other third remained untreated as control. A schematic illustration of the specimen preparation and amalgam restoration is provided in Figure 1.

All samples were stored for 24 hours in simulated body fluid solution (SBFS), pH 7.45, at 37 °C, and then submitted to the test of thermal cycling (100,000cy/5 °C and 55 °C, during 3 months) (SD Mechatronik GmbH, Germany), in PBS (phosphate buffered saline) (Ref. D8662, SIGMA-ALDRICH, St Louis, USA). The amalgam tiles were removed from the discs by cutting away the amalgam around the retentive pins.

### **Atomic Force Microscopy (AFM) analysis. Nanoroughness measurements**

The dentin surfaces were automatically polished wet (Struers LaboPol-4, Struers, Copenhagen, Denmark), using a series of SiC abrasive papers down to 4000 grits. Subsequently, they were polished with diamond pastes of 1 and 0.25  $\mu\text{m}$  on a hard cloth and, finally, finished by polishing with 0.05- $\mu\text{m}$  alumina powder slurry. The discs surfaces were scanned using an atomic force microscopy in tapping mode (TM/AFM) (Nanoscope V, Digital Instruments, Veeco Metrology Group, Santa Barbara, CA, USA). The tapping mode

was performed using a 1–10 Ohm-Cm phosphorus (n) doped Si tip. Changes in vertical position provide the height of the images, registered as bright and dark regions. The tip sample was maintained stable through constant oscillation amplitude. A data scale of 1,504  $\mu\text{m}$  and a slow scan rate (0.1 Hz) were employed. Five three-dimensional (3D) digital images (15 x 15  $\mu\text{m}$ ) were obtained from each specimen. To analyze the intertubular dentin surface nanoroughness, five randomized boxes (1 x 1  $\mu\text{m}$ ) were created on each topographical image (n = 75). Topography and the average surface nanoroughness (SRa nanometers) of the scanned areas were evaluated. All measurements were performed using Nanoscope Software V7. Nanoroughness values were analyzed by one-way ANOVA and Student- Newman-Keuls multiple comparisons tests.

### **X-Ray Diffraction (XRD) analysis**

The X-ray micro-diffractometer ( $\mu\text{XRD}^2$ ) used in this study was a single crystal diffractometer with a 2-dimensional detector system Cmos Photon 100 (Bruker-D8 Venture, Wien, Austria), equipped with kappa geometry based goniometer 2D Detector and XRD 2D Scan software. The X-ray beam (Cu  $K\alpha$  line,  $\lambda = 1.5418 \text{ \AA}$ ) was generated by a Cu Microforms source  $I_{\mu\text{s}}$  and generator settings of 50.00 kV/1.00 mA were employed. The 2D position sensitive detector had 1024x1024 pixels. Both the starting and ending positions were: distance, 40.00 mm;  $2\theta$ : 40.00°; Omega: 20.00°; Phi: 270.00°; Chi: 50.00°. Wavelength of 1.54184  $\text{\AA}$  (Cu). The sample to detector distance was 40.00 mm,  $2\theta$  scanning angle range was from 10° to 80°. All measurements were performed at room temperature ( $295\pm 0.1^\circ\text{K}$ ) and an exposure time of 60.00 s. A voltage of 50.00 kV, a current of 1.000 mA with the anode of Cu were used for the generator. The schematic illustration of the specimen preparation for XRD analysis, after the amalgam removal, is shown in Fig. 2. The rest of the procedure is as in Toledano et al. (2016).

From the X-ray micro-diffraction pattern, it has been calculated the size of the crystallites, the root-mean-square of the lattice strain and the crystallites preferred orientation. For this, it was proceeded as follows. First, Scherrer equation to calculate the crystallite size (Perales et al., 2008; Zhang et al., 2003; Xue et al., 2013), was used:

$$d = \frac{K\lambda}{\beta \cos \theta} \quad (1)$$

In this equation  $d$  is the mean size of the crystallites,  $K$  is a dimensionless shape factor, with a value close to unite –note that in the case of dentin,  $K \approx 0.94$  (Xue et al., 2013), and  $\beta$  is the peak full width at half maximum (FWHM) of the line broadening. In order to obtain the crystallite length and width, we used this formula for the line broadenings corresponding to 002 and 310 reflections, respectively (see data in Table 2).

Alternatively, the mean crystallite size, and also an estimation of the lattice strain, can be obtained by Scherrer-Wilson equation (Perales et al., 2008; Klug & Alexander, 1974; Xue et al., 2013):

$$\frac{\beta^2}{\tan^2 \theta} = \frac{1}{d} \frac{K\lambda\beta}{\tan \theta \sin \theta} + 20\varepsilon_{rms} \quad (2)$$

In this expression  $\varepsilon_{rms}$  is the root-mean-square of the lattice strain and the FWHM of the line broadening,  $\beta$ , is calculated by the following integral of the intensity,  $I$ , carried out

over the line broadening,  $\beta \approx \frac{1}{I_p} \int_{peak} I d\theta$ , with  $I_p$  being the peak intensity. In order to obtain

$d$  from equation (2), there have been then plotted the values of  $\frac{\beta^2}{\tan^2 \theta}$  as a function of

$\frac{K\lambda\beta}{\tan \theta \sin \theta}$  for the line broadening. By doing so, the experimental data were approximately

distributed along a straight line for all the samples under study (see Fig. 3 as an example) and,

thus, we could safely apply the Scherrer-Wilson model. Finally, it was obtained the slope and the intercept of the line of the best fit to the experimental data by performing a regression analysis using the method of least squares. From these data (slope and intercept), the crystallite size (equal to the inverse of the slope) and the root-mean-square of the lattice strain [(equal to the intercept) –see Table 2)], were also obtained. Note that the root-mean-square of the lattice strain is a measure of the local distortion of the lattice planes (Lewis & Northwood, 1968). As for Scherrer equation, the crystallite length and width by line broadenings corresponding to 002 (*H*) and 310 (*L*) reflections, respectively (see data in Table 2), have been calculated. In order to determine the interaction of variables with the HAp structure the ratio *H/L* (Bigi et al., 2004) was also measured.

Finally, it has been assessed the preferred orientation of the crystallites (texture) from the following intensity ratios (Xue et al., 2013):

$$R_{hkl} = k_{hkl} \frac{I_{211}}{I_{hkl}} \quad (3)$$

In this expression  $I_{211}$  and  $I_{hkl}$  are the intensities corresponding respectively to line reflections 211 and *hkl*, and  $k_{hkl} = \frac{I_{hkl}^{st}}{I_{211}^{st}}$ , where the superscript *st* refers to intensities calculated according to the JCPDS card. Note that *R* values close to unity correspond to random orientation, whereas *R* values significantly different than unity indicate the presence of preferred orientation of the crystallites in the crystallographic direction associated to the corresponding line reflection (Low, 2004; Xue et al., 2013).

## **Field Emission Scanning Electron Microscopy (FESEM) and energy dispersive (SEM/EDX) analyses**

Specimens were then fixed in a solution of 2.5% glutaraldehyde in 0.1 mol/L sodium cacodylate buffer for 24 h, rinsed three times in 0.1 mol/L sodium cacodylate buffer. Samples were placed in an apparatus for critical point drying (Leica EM CPD 300, Wien, Austria). They were then sputter-coated with carbon by means of a sputter-coating Nanotech Polaron-SEMPREP2 (Polaron Equipment Ltd., Watford, UK) and observed with a field emission scanning electron microscope (FESEM Gemini, Carl Zeiss, Oberkochen, Germany) at an accelerating voltage of 2.5 to 3 kV. Energy-dispersive analysis was performed in selected points using an X-ray detector system (EDX Inca 300, Oxford Instruments, Oxford, UK) attached to the FESEM.

## RESULTS AND DISCUSSION

Our results confirm that placing of Zn-containing restorations reduced crystallinity, crystallite size and grain size, increasing both microstrain and nanoroughness in caries-affected dentin, creating amorphous mineral for further functional remineralization.

X-ray diffraction patterns of dentin indicate that they are essentially constituted of HAp as a unique crystalline phase (Figs. 4 and 5). The analysis of  $\mu$ XRD<sup>2</sup> profiles of dentin (Fig. 5) showed that the physical broadening (FWHM) of peaks at 002 ( $2\theta$ , 25.900°; centroid peak position  $\theta_{hkl}$ , 0/0/-2; I, 10977386) and 310 ( $2\theta$ , 40.127°; centroid peak position  $\theta_{hkl}$ , -3/1/0; I, 1380390) reflections, were increasing in caries-affected dentin surfaces restored with both Zn-free (Fig. 4) and Zn-containing (Fig. 5) amalgams, after thermocycling. Mineral crystallinity (FWHM) merely expresses the crystallographic or relative atomic order obtained from diffractometry, since narrower peaks suggest less structural variation in bond distances and angles (Schwartz et al., 2012). In general, the narrower the spectral peak width is, the higher the degree of mineral crystallinity (Karan et al., 2009). This association denotes the presence of higher degrees of impurities and amorphous components, with decreased

chemical stability (Moshaverinia et al., 2008). It also creates biogenic apatites that are characterized by low degree of crystallinity and non-stoichiometry (Bigi et al., 2004).

At figure 8, the deposits of this new apatite at intertubular, peritubular and intratubular dentin may be pointed out, and it reveals that the analyzed surface is located at the subtransparent zone of the caries-affected dentin (Fusayama, 1993). In this zone, tubules are usually and partially occluded with mineral, but the amount of mineral at intertubular dentin might not be normal (Marshall et al., 1997). A non regular pattern of mineral crystallization was attained, as crystal deposits adopted microtubular-shaped organization (intratubular) or knob-like profiles (peritubular). Since calcium and phosphorous are the main components of biological apatite, these ions play an essential role in remineralization (Sauro et al., 2013; Toledano et al., 2012). The principal components that resulted after EDX analyses (Fig. 8, Ep6/Ep7) were phosphorus (P), calcium (Ca), magnesium (Mg), tin (Sn) and zinc (Zn). Both  $Zn^{2+}$  and  $Sn^{2+}$  perform as Ca/P growth inhibitor (Hoppe et al., 2011), favoring stabilization of the amorphous state (Barrère et al., 1999), and therefore, hindering crystallinity of the new nucleated minerals. The incorporation of  $Mg^{2+}$  implicates shortening of the c-axis and a reduction of crystallinity (Okazaki & LeGeros, 1992). Cl<sup>-</sup> appearance (Fig. 8, Ep6), though limited, has been linked to a lack of maturation (Hanschlin & Stern, 1995). Zinc may act as crystal growth inhibitor facilitating amorphous calcium phosphate stabilization, and intrafibrillar remineralization of collagen. Zinc stimulates remineralization as a direct activator of the enzyme alkaline phosphatase. Magnesium and zinc have also been shown to inhibit osteoclast activity, and induce new bone formation through regulation of osteoblast differentiation (Hoppe et al., 2011; Ma et al., 2013). It has also been demonstrated the inhibition of metalloproteinases by metals, metal salts, and zinc present in dental products. Zinc strongly reduced MMPs mediated collagen degradation in partially demineralized dentin. A collagen protector effect, exerted through binding at the collagen sensitive cleavage

sites of metalloproteinases, has been advocated, so metalloproteinases will be able to act in the subsequent remineralization process (Osorio et al., 2011).

Remineralization is a dynamic process in which amorphous phase formation, phase stabilization, and transition of calcium phosphate continuously occur (Ten Cate & Featherstone, 1996). This general lack of mineral maturity may influence some properties of the dentin surface. Authors agree that a roughness decrease may be associated to a role of mineral maturation (Zurick et al., 2013). The average roughness measurements determined from multiple AFM images for each dentin sample submitted to study are summarized in figure 10. When comparing the quantifiable surface roughness, a different trend from that seen for the non-treated group was found, *i.e.*, dentin surfaces restored with Zn-containing amalgams showed higher SRa than dentin surfaces restored with Zn-free amalgams or the control group, which performed similar. It is believed that the formation of specific mineral nodules at both sound and caries-affected dentin might have favored amorphous-bulk mineral precipitation. Beyond that, bulk precipitates may be more likely to settle not only into features on the sample surface, but in the presence of Zn within the chemical composition of the restorative, ultimately leading to an augmentation of the surface roughness (Zurick et al., 2013).

In dentin surfaces treated with Zn-free restorations and assessed at (002) reflections, caries-affected dentin attained ~5.24% lower FWHM than sound dentin. On the contrary, at (310) reflections, crystallinity decreased ~2.27%, indicating an increase in the crystal disorder of HAp, which has been associated to lower mechanical properties (Low, 2004). This clearly suggests that human dentin is a functionally graded material with a distinct gradation or heterogeneity in crystal disorder, at the nanometer and micrometer scale. The heterogeneous crystals distribution was observed in the FESEM analysis (Fig. 7), where multiple rhomboid-shape  $\beta$ -tricalcium phosphate mineral crystals of Whitlockite, plate like minerals or non-

regular mineral formations were spotted at the entrance of tubules. This location corresponded with the transparent zone of the caries-affected dentin substrate (Fusayama, 1993) where, additionally, some collagen fibers exhibited mineral deposits embedded in the remnant collagen scaffold-like structure (Fig. 7c).

When Zn-containing amalgams were evaluated, caries-affected dentin resulted  $\sim 1.91\%$  less crystalline (higher FWHM) than sound dentin at (002) reflections, and practically unchanged at (310) reflections (Table 2). It has been hypothesized that the lower sharp peaks or peak broadening (Zhang et al., 2003) perpendicular to the c-axes (Hansch & Stern, 1995) in the  $\mu\text{XRD}^2$  indicated that sound dentin became more amorphous (Moshaverinia et al., 2008) or with more crystals imperfections in nanocrystallite materials, *i.e.*, small crystallite size and lattice distortion (Zhang et al., 2003) than caries-affected dentin. In addition, sound dentin (Figs. 9e, 9f) resulted less rougher than caries-affected dentin (Fig. 10), and as a consequence it is a more mature tissue (Zurick et al., 2013); this counterargument needs further research. Those mineralized formations, though more crystalline (lower FWHM) (Table 2), were shown covering both the intertubular (Fig. 6a), and the peritubular (Fig. 6b) sound dentin. In a large extent, tubules appeared totally mineral-occupied with an advanced and complete hermetic sealing (Fig. 6a) of the dentin surface. The analysis of  $\mu\text{XRD}^2$  profiles (Fig. 4) permitted to observe an almost complete overlapping, in the range from  $\sim 49^\circ 2\theta$  to  $53^\circ 2\theta$  of traces corresponding to both sound and caries-affected dentin, involving the 213, 321, 410 and 404 peaks. The rest of the reflections attained relatively greater intensities in caries-affected dentin than in sound dentin, as shown in Table 2. The analysis of  $\mu\text{XRD}^2$  profiles comply with the depth profile 2-D  $\mu\text{XRD}^2$  scan frames of sound dentin (Fig. 4, inset a) and caries-affected dentin (Fig. 4, inset b) which showed continuous Debye-Scherrer rings at lower  $2\theta$  angles ( $40.00^\circ$ ). The diffraction rings corresponding to 211, 300, 201, 112 and 301 planes became comparatively overlapped and formed a tighter and intense ring in caries-

affected dentin than in sound dentin. A broader and less intense ring was created when 312, 213, 321, 410 and 402 planes overlapped (Fig. 4, inset b) in caries-affected dentin treated with Zn-free amalgam restorations. Relevant to  $\mu\text{XRD}^2$  analysis performed on dentin samples restored with Zn-containing amalgams, overlapping did not occur between  $\sim 25^\circ 2\theta$  to  $54^\circ 2\theta$  of traces, and peaks at 100, 101, 200, 111, 322, 313, 304 and 511 performed similar. Caries-affected dentin attained higher intensities than sound dentin in the rest of the reflections. The analysis of  $\mu\text{XRD}^2$  profiles merely comply with the depth profile 2-D  $\mu\text{XRD}^2$  scan frames of sound dentin (Fig. 5, inset a) and caries-affected dentin (Fig. 5, inset b) which showed continuous Debye-Scherrer rings at lower  $2\theta$  angles ( $40.00^\circ$ ), narrower but more intense than the ring seen in specimens treated with Zn-free amalgam restorations. The diffraction analysis formed brighter rings in both sound (Fig. 5, inset a) and caries-affected dentin (Fig. 5, inset b), indicating quasi similar line broadening of peaks, though  $2 \times 10^2$  counts sharper in carious dentin than in sound dentin (Fig. 5).

Crystallite size in calcified tissues has been shown to increase with tissue maturation (Hansch & Stern, 1995; Gawda et al., 2004). The crystallite size derived from Eqs. (1) and (2) is regarded as the size of the coherently diffracting domains, *i.e.*, coherent domain size is not limited to the grain sizes but may, frequently, include imperfections (stacking faults, twins, dislocations arrays, or small-angle boundaries) (Zhang et al., 2003). The stacking or twin faults can introduce additional broadening and peak shifting (Wagner, 1966). A qualitative estimation of the size of the coherently scattering domain (*i.e.* the crystallite size) is reported in Table 2.  $\tau_{002}$  ( $H$ ) is related to the mean crystallite size along the  $c$ -axis, whereas  $\tau_{310}$  ( $L$ ) refers to the mean crystallite size along a direction perpendicular to it (Bigi et al., 2004). Variability of the crystallites size through the length according to the type of restored dentin may be observed in Table 2. Caries-affected dentin ultimately showed the shortest mineral crystallites (11.04 nm), *i.e.*, the lesser needle shaped (decreased in average length)

when Zn-containing amalgams were used for restorations. On the other hand, sound dentin restored with Zn-free restorations exhibited a substantial increase in length of grain particles (12.44 nm) embedded into dentin crystallites (Table 2). This relative expansion of the lattice parameter could be a result of the practically negligible presence of  $Mg^{2+}$  at the EDX analysis (Fig. 6, Ep1/Ep2), with its incorporation within the lattice structure causing a shortening (Fig. 8, Ep7) (Hansch & Stern, 1995). Therefore, taking into account the present results, it is possible to *i*) clearly associate both lower crystallinity and contraction along the direction orthogonal to the *c*-axis in caries-affected surfaces when Zn-containing amalgam restorations were used, and *ii*), to partially assume that the observed decreasing degree of thickness of crystallites, in caries-affected dentin restored with Zn-containing amalgams (6.26 nm), fits with a decrease in mineralization and maturity, as well as increase in nanoroughness (Fig. 10); all these may explicitly be related to a decrease in mechanical properties (Xue et al., 2013). However, this hypothesis requires further research.

After  $\tau_{310}$  (*L*) analysis it was demonstrated a reduction in thickness (~1.75 fold) of crystallites assessed in caries-affected dentin below Zn-containing amalgams when samples were compared with the untreated group (Table 2). Therefore, those crystallites ultimately became less platy (decreased in average width). This lack of maturation procedure corresponded with broadening of peaks (~1.76) fold, with FWHM increasing up to 1.740. Additionally, the contraction of the lattice parameters might also be related to the incorporation of carbonate as substituent for  $PO_4^{3-}$  in the apatite lattice (Hansch & Stern, 1995). It has been previously reported that the incorporation of carbonate, expressed as augmentation of both *i*) relative mineral concentration between mineral/phenyl and *ii*) gradient in mineral content (carbonate/phosphate), weakens the crystallinity (Toledano et al., 2015a). Apart from that, the *H/L* ratio is slightly greater for the group of caries-affected dentin restored with Zn-containing amalgams (1.76) if compared to carious dentin treated

with Zn-free amalgam restorations (Table 2). This suggests a stronger interaction of Zn-containing amalgam with the HAp structure of the carious tissue (Bigi et al., 2004). Nevertheless, crystallite thickness as determined by Scherrer equation has shown comparable width data (6.1 nm in sound dentin, control group) with those obtained by Kinney et al. (2001) who reported ~5.0 nm thickness. It is important to remark that the slight variation in crystalline thickness was referred to both reflections (002) and (310). It has been argued that crystal growth is constrained in one axis, where concretely the thickness would be limited to the width of the 67-nm gap zone in the collagen fibril. This gap zone is precisely primary site for apatite crystal nucleation and growth (Kinney et al., 2001).

The ultrastructural observations confirmed that the grain size, expressed throughout the Scherrer-Wilson equation, of dentin crystals became smaller (~1.08 fold) in caries-affected dentin restored with Zn-containing amalgams (9.34 nm) than in sound dentin of the untreated group (10.05 nm) (Table 2), at (002) reflections. At (310) reflections this decrease was ~1.21 fold bigger. Grain size and lattice microstrain accordingly can be determined by measuring the deviation of line profile from perfect crystal diffraction (Zhang et al., 2003). The diffraction lines can be considered as the convolutions of two hypothetical functions that depend on the two factors: the crystalline form and size, and the microstrain of the lattice. The crystallites are essentially the regions in the specimen diffracting X-rays coherently and independently, whereas the strain is due to different displacement of the atoms with respect to their reference position in a perfect lattice. Size broadening is independent from the order of the reflection, whereas strain broadening is precisely order-dependent (Bigi et al., 2004).

Microstrain was measured as the change in d-spacing of a strained sample compared to the unstrained state of a perfect or standard crystal (Hansch & Stern, 1995), and calculated from (002) and (310) was tensile for all crystallites, in dentin. The lattice strain within the long dimension (002 reflection) of the dentin crystals, in caries-affected dentin

restored with Zn-containing amalgam, increased ~1.16 fold, respect to the control group, but decreased ~1.32 fold respect to sound dentin restored with Zn-containing amalgam (Table 2). As a result, most strain was concentrated in restored sound dentin when Zn-containing amalgams were used for restoration ( $5.0 \times 10^{-6}$ ) (Table 2). These increased strain values were primarily responsible for the broadening of diffraction peaks (0.820) even in the presence of the lowest grain size (8.11 nm) (Bigi et al., 2004). At (310) reflections, the greater microstrain ( $10.9 \times 10^{-6}$ ) and the lowest grain (5.96 nm) and crystallite size (6.27 nm) were likewise achieved at sound dentin, within the group of samples restored with Zn-containing amalgams (Table 2). The different mean crystallite sizes obtained are ultimately due to the contribution of the strain to the broadening of the diffraction peaks (Bigi et al., 2004). In addition to this, a peak broadening may be a result of a significant organic fraction in dentin (Gawda et al., 2004), characteristic of caries-affected dentin substratum (Marshall et al., 1997). Nano-sized crystallites normally show high surface energy, which increases with the reduction of the size of the crystallites and therefore results in the presence of uniform and nonuniform strain in the particles (Xue et al., 2013). An important role of dentin is transferring mastication and other types of stresses through the buccal and lingual sides of enamel into coronal dentin through mid-way between the cusp tip and the cervical margin onto root dentin (Goel et al., 1991; Xue et al., 2013). The stress distribution on the surface of dentin cause cracks (Fujisaki et al., 2012). It is speculated that the present combination of crystallographic properties might favor crack propagation and deformation (Xue et al., 2013). The discrepant viscoelastic properties obtained between peritubular and intertubular dentin in caries-affected substrata restored with Zn-containing amalgam indicate the clear augmentation of the stress concentration within the peritubular cuff. This stress may initiate or exacerbate failures which might dissipate through cracking the dentin substrate altering the transfer of energy, with implications for dentin remineralization and remodeling (Toledano et al., 2015c). At tubular structures, energy

dissipation occurs via deformation in axial and radial directions (Agrawal et al., 2013), as validated from FESEM images (Fig. 8). It has been stated that tubular system suppress failure through crack-bridging and frictional pullout (Agrawal et al., 2013), nucleating minerals at micro and nano-scale damaged zones. Those mineral formations maintained anchored directly or indirectly (crack-bridging) the intratubular deposits of minerals to the peritubular dentin (Figs. 8, 9f), and represents a lack of hermetic sealing favoring future micropermeability. Those failures can correlate with the crystalline texture.

Texture is the distribution of crystallographic orientation of a polycrystalline sample. It is related to changes in microstructure, showing a great influence on materials properties, as cracking resistance (Liss et al., 2003). Texture indices ( $R_{hkl}$ ) in dentin polycrystalline structures were calculated according to Eq. (3). For  $R \approx 1$ , the grains were considered randomly oriented (Xue et al., 2013). This criterion was only followed by the group of caries-affected dentin restored with Zn-free amalgams (Table 2), at the 002 plane; thereby, this group did not show almost any distinct texture (Liss et al., 2003).  $R$  values greater or lower than 1.0 indicate the presence of preferred grain orientation or texture (Low, 2004). The degree is dependent on the percentage of crystals having the preferred orientation (Liss et al., 2003). A  $R$  rising was obtained by the carious dentin restored with Zn-containing amalgams. Texture indices corresponding to the reflections (002) were greater than 1 (1.164) (Table 2). That indicates the preferred orientation of the crystallites in the crystallographic direction, at these planes (Low, 2004; Xue et al., 2013). They also exhibited a perpendicular alignment to the occlusal surface, as  $R$  values are greater than 1.0 (Low, 2004). On the contrary, at the reflections (310) all assessments resulted lower than 1.0 ( $R < 1$ ), but all groups showed less variation than at (002) reflection, *i.e.*, less nanodegradation for the later (Low, 2004). Only caries-affected dentin restored with Zn-containing amalgams showed the texture nearest (0.607) to the randomly orientation (Table 2). As  $R$  values are less than 1.0, crystallites are

aligned parallel to the occlusal surface (Low, 2004). In addition, the scarce variation of R values within this reflection mode (310) suggest the existence of a modest gradation in texture at the nanometer scale within the complex dentin microstructure, indicating poor three-dimensional interlocking HAp structure to withstand strength and provide both hardness and stress-bearing capability (Low, 2004). Thus, any fracture or strong discontinuity in the mechanical properties at the microscopic level of the restoration, restorative interface of dental substrate would definitely have consequences in the overall function that takes place at the macroscopic level (centimeter length scale). The dependence of crystallite sizes on crystallographic orientation may arise from the fact that crystallites of the bulk may not be completely random oriented; as a result, the dimension variation in the crystallographic orientation may imply that the grains are not quite equiaxed; furthermore, the presence of texture may have contributed to the larger difference of the grain sizes among the two reflections (Zhang et al., 2003). Therefore, from the results described above, it appears that the degree of crystal disorder in HAp may be related to its crystal size. For this reason, future complementary TEM studies are required to exactly determine encountered variations in crystallographic orientation. It is further proposed (Low, 2004) that the degree of hydroxylation or the incorporation of  $\text{OH}^-$  within the HAp decreases as the crystal size decreases. A lack of  $\text{OH}^-$  in nanocrystalline HAp is believed to cause crystal disorder.  $\text{OH}^-$  ions are more readily incorporated into apatites with a large crystal lattice which induces the polar nature of the HAp. Polarity is crucial for the high degree of alignment of crystallites. This lack of both  $\text{OH}^-$  and polarity is believed to result in their random alignment and thus a high degree of crystal disorder. It appears that nature imposes a specific state of crystal disorder by varying the concentration of  $\text{OH}^-$  to enhance the ability of biological apatites to carry out their tissue-specific functions (Pasteris et al., 2004).

## SUMMARY

These are, to the best of our knowledge, the only available results from remineralization experiments through  $\mu$ XRD<sup>2</sup> analysis on partially mineral-depleted substratum in caries-affected dentin surfaces restored with Zn-free *vs* -containing amalgams. To sum up, these outcomes permit to assume that when caries-affected dentin surfaces were analyzed through  $\mu$ XRD<sup>2</sup> after Zn-containing removal restorations, the provoked broadening and the decreased crystallinity that were attained resulted associated to, *i*) a reduced crystallite size in length and width, *ii*) increased microstrain, texture (Table 2) and nanoroughness (Fig. 10), and as result to a more amorphous dentin substrate, when compared with the untreated group. As a result, the null hypothesis which reads that there are no differences in physical and morphological characteristics of sound and caries-affected substrata after removal of Zn-free *vs* containing amalgam restorations, should be rejected. It is important to emphasize that amorphous Ca/P provides a local ion-rich environment which is considered favorable for *in situ* generation of prenucleation clusters, succeeding further dentin remineralization (Liu et al., 2011). A diagrammatic model, summarizing the main outcomes that were obtained is included in the Figure 11. On the contrary, if crystalline calcium phosphates are formed, they will have long degradation times, requiring months or even years to provide ions to the remineralizing media (Rezwan et al., 2006). The biodegradability of these new mineral formations explicitly depends on many parameters such as crystallinity, porosity, chemical purity, surface roughness, pH in the media, and other solubilized ions present in the biological fluid at the oral environment (Hoppe et al., 2011; Cochrane et al., 2010). Therefore, to correlate our present technique with complementary chemical tests is recommended for future strategies of research. Further work is also required to determine the mechanism by which thermal cycling prevents mechanical and thermal induced changes in dentin mineralization and dentin strength. Finally, Warren-Averbach's approach by using the WinFit program

should be considered in future research, in order to enable separation of the contributions of the crystallite sizes from strain, although it considers each diffraction peak separately and it does not take into account the crystallite shape.

## **ACKNOWLEDGEMENTS**

This work was supported by grants MINECO/FEDER MAT2014-52036-P and FIS2013-41821-R. The authors have no financial affiliation or involvement with any commercial organization with direct financial interest in the materials discussed in this manuscript. Any other potential conflict of interest is disclosed.

## REFERENCES

- AGRAWAL, R., NIETO, A., CHEN, H., MORA, M. & AGARWAL, A. (2013). Nanoscale Damping Characteristics of Boron Nitride Nanotubes and Carbon Nanotubes Reinforced Polymer Composites. *ACS Appl Mater Interfaces* **5**, 12052-12057.
- BARRÉRE, F., LAYROLLE, P., VAN BLITTERSWIJK, C.A. & DE GROOT, K. (1999). Biomimetic calcium phosphate coatings on Ti6Al4V: a crystal growth study of octacalcium phosphate and inhibition by Mg<sup>2+</sup> and HCO<sub>3</sub><sup>-</sup>. *Bone* **25**, 107S-111S.
- BERTASSONI, L.E., HABELITZ, S., KINNEY, J.H., MARSHALL, S.J. & MARSHALL JR., G.W. (2009). Biomechanical Perspective on the Remineralization of Dentin. *Caries Res* **43**, 70-77.
- BIGI, A., BOANINI, E., GAZZANO, M., KOJDECKI, M. A. & RUBINI, K. (2004). Microstructural investigation of HAp–polyelectrolyte composites. *J Mater Chem* **14**, 274-279.
- COCHRANE, N.J., CAI, F., HUQ, N.L., BURROW, M.F. & REYNOLDS, E.C. (2010). New Approaches to Enhanced Remineralization of Tooth Enamel. *J Dent Res* **89**, 1187-1197.
- FUJISAKI, K., TODOH, M., NIIDA, A., SHIBUYA, R., KITAMI, S. & TADANO, S. (2012). Orientation and deformation of mineral crystals in tooth surfaces. *J Mech Behav Biomed Mater* **10**, 176-182.
- FUSAYAMA, T. (1993). *New concepts in the pathology and treatment of dental caries*. St Louis: Ishiyaku EuroAmerica Inc. pp. 1-21.
- GAWDA, H., SEKOWSKI, L. & TREBACZ, H. (2004). In vitro examination of human teeth using ultrasound and X-ray diffraction. *Acta Bioeng Biomech* **6**, 41-50.

- GOEL, V.K., KHERA, S.C., RALSTON, J.L. & CHANG, K.H. (1991). Stresses at the dentinoenamel junction of human teeth--a finite element investigation. *J Prosthet Dent* **66**, 451-459.
- HABELITZ, S., MARSHALL, S.J., MARSHALL, G.W. & BALOOCH, M. (2001). The functional width of the dentino-enamel junction determined by AFM-based nanoscratching. *J Struct Biol* **135**, 294-301.
- HANSCHIN, R.G. & STERN, W.B. (1995). X-ray diffraction studies on the lattice perfection of human bone apatite (Crista iliaca). *Bone* **16**, 355S-363S.
- HOPPE, A., GÜLDAL, N.S. & BOCCACCINI, A.R. (2011). A review of the biological response to ionic dissolution products from bioactive glasses and glass-ceramics. *Biomaterials* **32**, 2757-2774.
- KARAN, K., YAO, X., XU, C. & WANG, Y. (2009). Chemical profile of the dentin substrate in non-carious cervical lesions. *Dent Mater* **25**, 1205-1212.
- KAY, M.I., YOUNG, R.A. & POSNER, A.S. (1964). Crystal Structure of HAp. *Nature* **204**, 1050-1052.
- KINNEY, J.H., OLIVEIRA, J., HAUPT, D.L., MARSHALL, G.W. & MARSHALL, S.J. (2001). The spatial arrangement of tubules in human dentin. *J Mater Sci Mater Med* **12**, 743-751.
- KLUG, H.P. & ALEXANDER, L.E. (1974). *X-Ray Diffraction Procedures for Polycrystalline and Amorphous Materials*. Wiley, New York.
- LEGEROS, R.Z. (1990). Chemical and crystallographic events in the caries process. *J Dent Res* **69** Spec No, 567-574; discussion 634-636.
- LEWIS, D. & NORTHWOOD, D.O. (1968). X-ray diffraction measurement of microstrains. *Strain* **4**, 19-23.

- LISS, K.D., BARTELS, A., SCHREYER, A. & CLEMENS, H. (2003). High energy X-rays: A tool for advanced bulk investigations in materials science and physics. *Textures Microstruct* **35**, 219-252.
- LIU, Y., TJADERHANE, L., BRESCHI, L., MAZZONI, A., LI, N., MAO, J., PASHLEY, D.H. & TAY, F.R. (2011). Limitations in Bonding to Dentin and Experimental Strategies to Prevent Bond Degradation. *J Dent Res* **90**, 953-968.
- LOW, I.M. (2004). Depth-Profiling of Crystal Structure, Texture, and Microhardness in a Functionally Graded Tooth Enamel. *J Am Ceram Soc* **87**, 2125-2131.
- MA, X.N., ZHOU, J., GE, B.F., ZHEN, P., MA, H.P., SHI, W.G., CHENG, K., XIAN, C. & CHEN, K.M. (2013). Icariin Induces Osteoblast Differentiation and Mineralization without Dexamethasone in Vitro. *Planta Med* **79**, 1501-1508.
- MARSHALL, G.W., MARSHALL, S.J., KINNEY, J.H. & BALOOCH, M. (1997). The dentin substrate: structure and properties related to bonding. *J Dent* **25**, 441-458.
- MAZZITELLI, C., MONTICELLI, F., TOLEDANO, M., FERRARI, M. & OSORIO, R. (2012). Effect of thermal cycling on the bond strength of self-adhesive cements to fiber posts. *Clin Oral Investig* **16**, 909-915.
- MORASCHINI, V., FAI, C.K., ALTO, R.M. & DOS SANTOS, G.O. (2015). Amalgam and resin composite longevity of posterior restorations: A systematic review and meta-analysis. *J Dent* **43**, 1043-1050.
- MOSHAVERINIA, A., ANSARI, S., MOSHAVERINIA, M., ROOHPUR, N., DARR, J.A. & REHMAN, I. (2008). Effects of incorporation of HAp and fluoroapatite nanobioceramics into conventional glass ionomer cements (GIC). *Acta Biomater* **4**, 432-440.
- OKAZAKI, M. & LEGEROS, R.Z. (1992). Crystallographic and chemical properties of Mg-containing apatites before and after suspension in solutions. *Magnes Res* **5**, 103-108.

- OSORIO, R., YAMAUTI, M., OSORIO, E., ROMÁN, J.S. & TOLEDANO, M. (2011). Zinc-doped dentin adhesive for collagen protection at the hybrid layer: Zinc-doped dental adhesive. *Eur J Oral Sci* **119**, 401-410.
- PASTERIS, J.D., WOPENKA, B., FREEMAN, J.J., ROGERS, K., VALSAMI-JONES, E., VAN DER HOUWEN, J.A. & SILVA, M.J. (2004). Lack of OH in nanocrystalline apatite as a function of degree of atomic order: implications for bone and biomaterials. *Biomaterials* **25**, 229-238.
- PERALES, F. DE LAS HERAS, C. & AGULLÓ-RUEDA, F. (2008). Structural properties of MgP<sub>2</sub> and ZnS in thin film and in multilayer optical coatings. *J Phys D: Appl Phys* **41**, 225405.
- QVIST, V., QVIST, J. & MJÖR, I.A. (1990). Placement and longevity of tooth-colored restorations in Denmark. *Acta Odontol Scand* **48**, 305-311.
- REZWAN, K., CHEN, Q.Z., BLAKER, J.J. & BOCCACCINI, A.R. (2006). Biodegradable and bioactive porous polymer/inorganic composite scaffolds for bone tissue engineering. *Biomaterials* **27**, 3413-3431.
- SAURO, S., OSORIO, R., OSORIO, E., WATSON, T.F. & TOLEDANO, M. (2013). Novel light-curable materials containing experimental bioactive micro-fillers remineralise mineral-depleted bonded-dentine interfaces. *J Biomater Sci Polym Ed* **24**, 940-956.
- SCHWARTZ, A.G., PASTERIS, J.D., GENIN, G.M., DAULTON, T.L. & THOMOPOULOS, S. (2012). Mineral Distributions at the Developing Tendon Enthesis. *PLoS ONE* **7**, e48630.
- SJÖGREN, P. & HALLING, A. (2002). Survival time of Class II molar restorations in relation to patient and dental health insurance costs for treatment. *Swed Dent J* **26**, 59-66.

- TEN CATE, J.M. & FEATHERSTONE, J.D.B. (1996). Physicochemical aspects of fluoride-enamel interactions. In *Fluoride in Dentistry*, Fejerskov, O., Ekstrand, J. & Burt, B.A. (Eds.), pp.187-213. Munksgaard Textbook, Copenhagen.
- TOLEDANO, M., YAMAUTI, M., RUIZ-REQUENA, M.E. & OSORIO, R. (2012). A ZnO-doped adhesive reduced collagen degradation favouring dentine remineralization. *J Dent* **40**, 756-765.
- TOLEDANO, M., SAURO, S., CABELLO, I., WATSON, T. & OSORIO, R. (2013). A Zn-doped etch-and-rinse adhesive may improve the mechanical properties and the integrity at the bonded-dentin interface. *Dent Mater* **29**, e142-e152.
- TOLEDANO, M., OSORIO, E., AGUILERA, F.S., TOLEDANO-OSORIO, M., LÓPEZ-LÓPEZ, M.T. & OSORIO, R. (2015a). Stored potential energy and viscoelastic properties alterations after restoring dentin with Zn-containing materials. *J Mech Behav Biomed Mater*. In press.
- TOLEDANO, M., AGUILERA, F.S., OSORIO, E., CABELLO, I., TOLEDANO-OSORIO, M. & OSORIO, R. (2015b). Mechanical and chemical characterisation of demineralized human dentine after amalgam restorations. *J Mech Behav Biomed Mater* **47**, 65-76.
- TOLEDANO, M., AGUILERA, F.S., OSORIO, E., LÓPEZ-LÓPEZ, M.T., CABELLO, I., TOLEDANO-OSORIO, M. & OSORIO, R. (2015c). On modeling and nanoanalysis of caries-affected dentin surfaces restored with Zn-containing amalgam and in vitro oral function. *Biointerphases* **10**, 041004.
- TOLEDANO, M., AGUILERA, F.S., OSORIO, E., LÓPEZ-LÓPEZ, M.T., CABELLO, I., TOLEDANO-OSORIO, M. & OSORIO, R. (2016). Submicron-to-nanoscale structure characterization and organization of crystals in dentin bioapatites. *RSC Adv* **6**, 45265.
- VASEENON, S. (2011). *Relationship between caries-affected dentin mineral density and microtensile bond strength*. Master's thesis. University of Iowa.

- WAGNER, C.N.J. (1966). Analysis of the Broadening and Changes in Position of Peaks in an X-Ray Powder Pattern. In *Local Atomic Arrangements Studies by X-ray Diffraction*, Cohen, J.B. & Hilliard, J.E. (Eds.), Metallurgical Society Conferences **36** pp. 219-268. New York: Gordon and Breach Science Publishers.
- XUE, J., ZHANG, L., ZOU, L., LIAO, Y., LI, J., XIAO, L., & LI, W. (2008). High-Resolution X-Ray Microdiffraction Analysis of Natural Teeth. *J Synchrotron Radiat* **15**, 235-238.
- XUE, J., ZAVGORODNIY, A.V., KENNEDY, B.J., SWAIN, M.V. & LI, W. (2013). X-ray microdiffraction, TEM characterization and texture analysis of human dentin and enamel. *J Microsc* **251**, 144-153.
- ZHANG, Z., ZHOU, F. & LAVERNIA, E.J. (2003). On the analysis of grain size in bulk nanocrystalline materials via X-ray diffraction. *Metall Mater Trans* **34A**, 1349-1355.
- ZURICK, K.M., QIN, C. & BERNARDS, M.T. (2013). Mineralization induction effects of osteopontin, bone sialoprotein, and dentin phosphoprotein on a biomimetic collagen substrate. *J Biomed Mater Res A* **101A**, 1571-1581.

## Legend of Figures

**Figure 1.** Schematic illustration of the specimen preparation and amalgam restoration, with an image of a restored disc.

**Figure 2:** Schematic illustration of the specimen preparation for XRD analysis, after the amalgam removal.

**Figure 3.** Example of the plot of  $\frac{\beta^2}{\tan^2 \theta}$  as a function of  $\frac{K\lambda\beta}{\tan \theta \sin \theta}$  for a line

broadening. As observed, the experimental points are distributed along a straight line.

**Figure 4.** Refined  $\mu\text{XRD}^2$  profiles of sound and caries-affected dentin after removal of Zn-free amalgam restorations. The corresponding Debye-Scherrer rings are shown in inset a (sound dentin/SD) and b (caries-affected dentin/CAD). Vertical bars represent HAp peaks.

**Figure 5.** Refined  $\mu\text{XRD}^2$  profiles of sound and caries-affected dentin after removal of Zn-containing amalgam restorations. The corresponding Debye-Scherrer rings are shown in inset a (sound dentin/SD) and b (caries-affected dentin/CAD). Vertical bars represent HAp peaks.

**Figure 6. (a):** FESEM image and EDX spectrum of sound dentin after removal of Zn-free amalgam restoration. Peritubular (PD) and intertubular (ID) dentin were strongly mineralized. A consistent mineral plug was observed occluding most of the dentinal tubules, and covering the peritubular dentin (asterisk). Some tubules appeared mineral free with a clear ring of peritubular dentin (arrow). Ep1 is an EDX spectrum at intertubular dentin indicating presence of phosphorous (P), calcium (Ca) and magnesium (Mg). **(b):** FESEM image and EDX spectrum of thermocycled sound dentin after removal of Zn-free amalgam restoration. Peritubular (PD) and intertubular (ID) dentin appeared clearly mineralized. Plate-like crystals formed the surface of

intertubular dentin. A robust and rougher peritubular dentin wall was observed (pointer). A mineral flat perforated plug occluded the bottom of the lumen of the tubule (arrow). Ep2 is an EDX spectrum, corresponding to peritubular dentin location, indicating presence of phosphate (P), calcium (Ca) and magnesium (Mg), among the principal components.

**Figure 7. (a):** FESEM image and EDX spectrum of caries-affected dentin after removal of Zn-free amalgam restoration. The typical character as a rhomboid-shape crystals, Whitlockite crystals (arrow), and a mineral plug (pointer) are occupying the lumen of the tubule. A strong collar of peritubular dentin may be shown (PD). Ep3 is an EDX spectrum, corresponding to intratubular dentin location, indicating presence of phosphate (P), calcium (Ca) and magnesium (Mg), among the principal components. **(b):** FESEM image and EDX spectrum of thermocycled caries-affected dentin after removal of Zn-free amalgam restoration. Irregular (pointer), larger (asterisk) or plate-like mineral (arrow) of Whitlockite crystals are located within the tubule. These Whitlockite crystals are occluding the dentinal tubule. A mineral platform is covering the rest of the dentin surface, though a portion of peritubular dentin may still be observed (PD). Ep4 is an EDX spectrum, corresponding to peritubular dentin location, indicating presence of phosphate (P), calcium (Ca) and magnesium (Mg), among the principal components. **(c):** FESEM image and EDX spectrum of thermocycled caries-affected dentin after removal of Zn-free amalgam restoration. A relevant peritubular ring is partially occluding the dentinal tubule. Granular (pointer), incomplete rhomboid-shape (asterisk) or plate-like mineral (double arrow) of Whitlockite crystals are located within the tubule and partially covered by the mineral platform. Some fibers appeared longitudinally mineralized, and the typical staggered pattern of collagen, due to the characteristic D- periodicity (67 nm), was visible at bigger magnifications (arrows).

**Figure 8.** FESEM image and EDX spectrum of caries-affected dentin after removal of Zn-containing amalgam restoration. Peritubular (PD) and intertubular dentin (ID) are clearly differentiated. Intratubular dentin appeared totally mineralized. Complete (single arrow) or partial (double arrow) mineral plugs were discernible. Coralline microtubular-shaped formations were also observed occupying the lumen of tubules (pointers). Some rod-like new mineral formations were observed surrounding the intratubular crystals. These mineral beams maintained directly (empty arrow) or indirectly (double empty arrows) anchored the intratubular deposits of mineral to the peritubular dentin. Mineralized clusters also appeared covering, partially, the peritubular dentin (faced arrows). A single layer of minerals covered the intertubular dentin and some extension of the peritubular dentin (asterisks). These crystal formations did not permit to see the subjacent collagen fibers. Ep6 and Ep7 are two EDX spectra, corresponding to intratubular and peritubular dentin locations, indicating presence of phosphate (P), calcium (Ca), magnesium (Mg), tin (Sn) and zinc (Zn), among the principal components.

**Figure 9.** AFM images of untreated sound (a) and caries-affected (b) dentin. Both images show a 15 x 15  $\mu\text{m}$  surface plot image of the dentin surface. Peritubular dentin is present (arrows) or absent (pointers). Partially demineralized collagen fibrils (asterisk), and extended mineral-depleted areas (double arrow) are reflected. Sound (c) and caries-affected (d) dentin after Zn-free amalgam removal, and thermocycling. Both images show a 15 x 15  $\mu\text{m}$  surface plot image of the dentin surface. Mineral tubular occlusion (arrow), and rod-like new minerals or “stick-slip” formations (pointers) were unveiled. Mineralized tubules appeared at the dentin surface (asterisk), and strong peritubular rings were formed at the entrance of some tubules (double arrows). Sound (e) and caries-affected (f) dentin after Zn-containing amalgam removal, and thermocycling.

Both images show a 15 x 15 µm surface plot image of the dentin surface. Multiple “stick-slip” formations (pointers) appeared covering a large extension of the intertubular dentin, and some extent of the peritubular dentin. Robust collars of mineralized dentin crowned the entrance of tubules. Some of these tubules figured completely occluded (arrow). A large platform of intertubular dentin (asterisks) protruded over the absent peritubular dentin, when this "turbid zone" of the carious dentin was analyzed. Some intratubular deposits partially occluded the lumen of tubules (double arrows).

**Figure 10.** Mean and standard deviation of nanoroughness SRa (nm) measured on sound and caries-affected dentin surfaces, after removal of Zn-free or Zn-containing amalgam restorations. Identical letters (lower case for sound dentin and capital for caries-affected dentin) indicate no significant differences after Student–Newman–Keuls test ( $p > 0.05$ ). \* indicates significant differences between sound dentin and caries-affected dentin, within the same amalgam group. Abbreviations: SD: sound dentin, CAD: caries-affected dentin.

**Figure 11:** Diagrammatic model showing a scheme of the most remarkable results and conclusions.

**Table 1.** Composition of amalgams used in the present study.

<b>AMALGAM</b>	<b>COMPOSITION</b>	
	<b>Alloy powder</b>	<b>Weight %</b>
Megalloy EZ®* (Zn-free)	Silver	56.7 %
	Tin	28.6 %
	Copper	14.7%
The recommended alloy to mercury ratio by mass is approximately 1.3:1		
Dispersalloy®* (Zn-containing)	Silver	69 %
	Tin	18 %
	Copper	12 %
	Zinc	1 %
The recommended alloy to mercury ratio by mass is approximately 1:1		

\* Dentsply Detrey GmbH Konstanz, Germany.

Table 2: Whole X-ray microdiffraction (XRD) pattern analysis approach of sound (SD) and caries-affected dentin (CAD).

Amalgam treatment	Dentin area	002 plane					310 plane					H/L
		FWHM	H: Scherrer equation (nm) ( $\tau$ )	Scherrer-Wilson equation (nm)	Microstrain %	$R_{hkl}$	FWHM	L: Scherrer equation (nm) ( $\tau$ )	Scherrer-Wilson equation (nm)	Microstrain %	$R_{hkl}$	
Untreated	SD	0.758	12.16	7.40	$7.9 \times 10^{-6}$	0.639	1.777	6.10	6.44	$9.3 \times 10^{-6}$	0.358	1.99
	CAD	0.605	15.25	10.05	$4.3 \times 10^{-6}$	0.741	0.986	11.00	8.06	$5.9 \times 10^{-6}$	0.536	1.39
Zn-Free	SD	0.783	11.80	10.17	$4.2 \times 10^{-6}$	0.822	1.470	7.36	5.38	$13.2 \times 10^{-6}$	0.523	1.60
	CAD	0.742	12.44	9.38	$4.9 \times 10^{-6}$	0.969	1.504	7.17	7.46	$6.9 \times 10^{-6}$	0.571	1.74
Zn-Containing	SD	0.820	11.25	8.11	$6.6 \times 10^{-6}$	1.140	1.739	6.27	5.96	$10.9 \times 10^{-6}$	0.593	1.79
	CAD	0.836	11.04	9.34	$5.0 \times 10^{-6}$	1.164	1.740	6.26	6.65	$8.6 \times 10^{-6}$	0.607	1.76

FIGURE 1

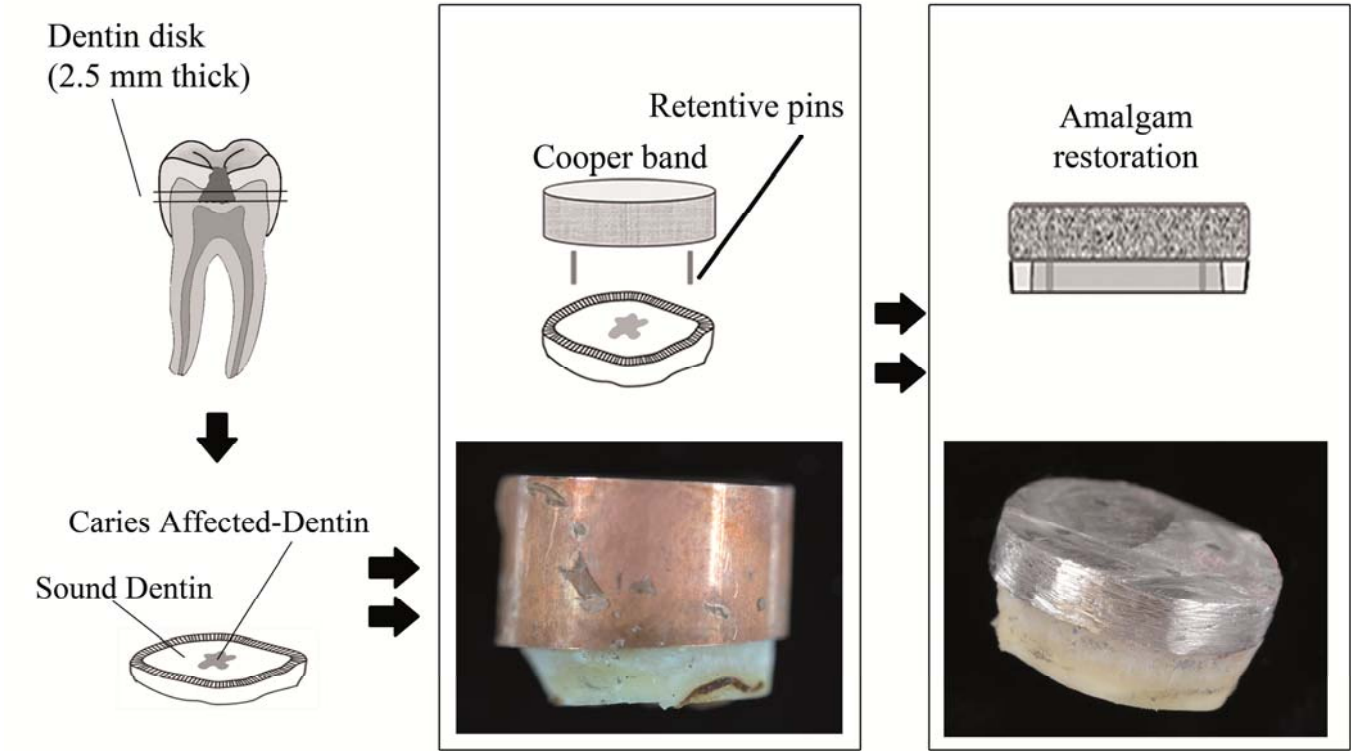


**FIGURE 2**

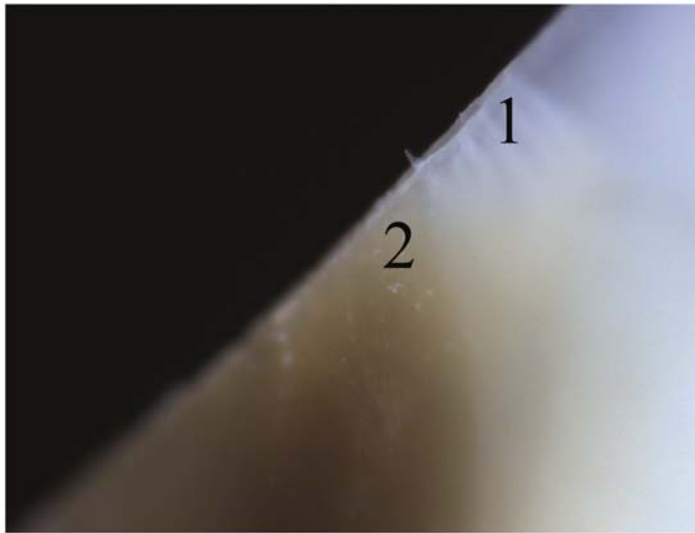


**FIGURE 3**

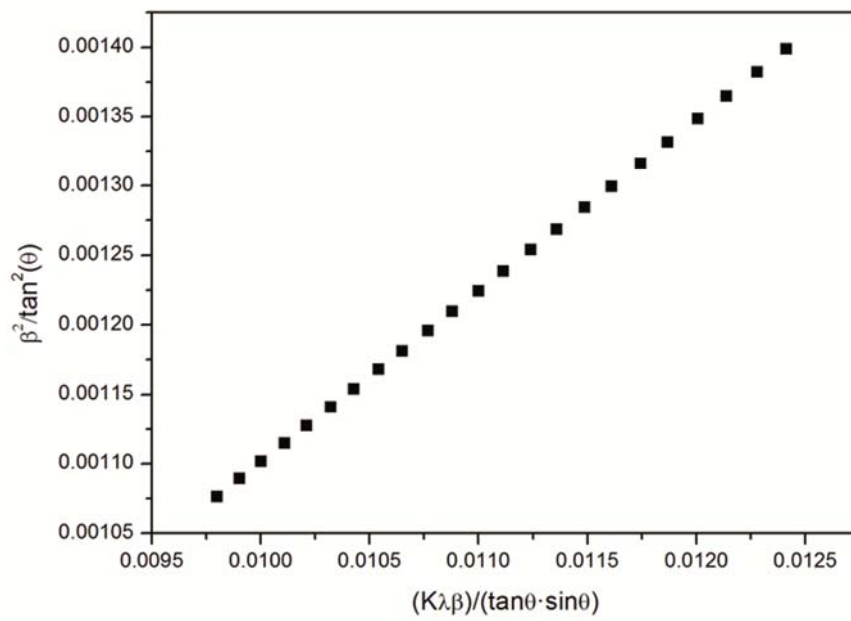


FIGURE 4

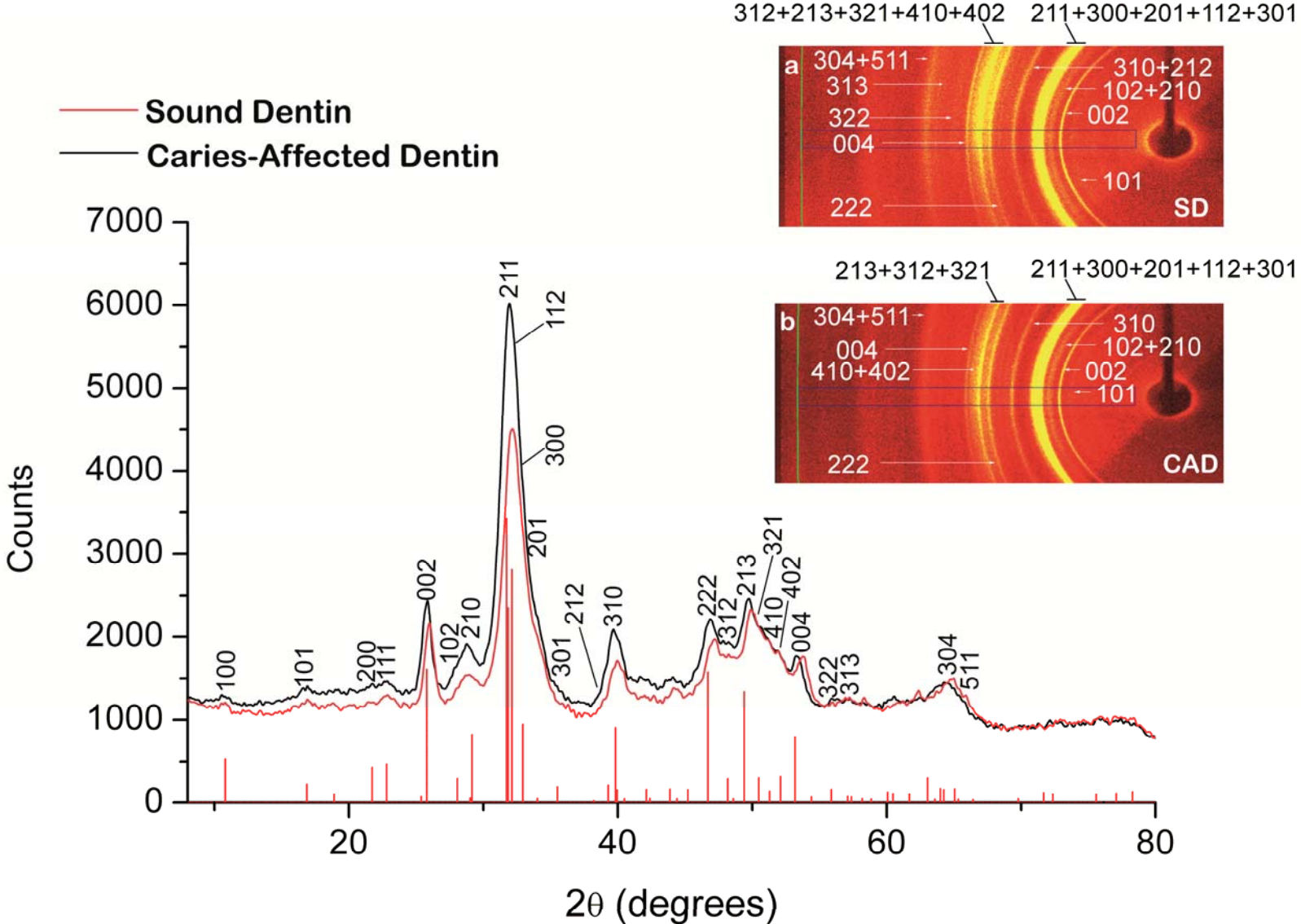


FIGURE 5

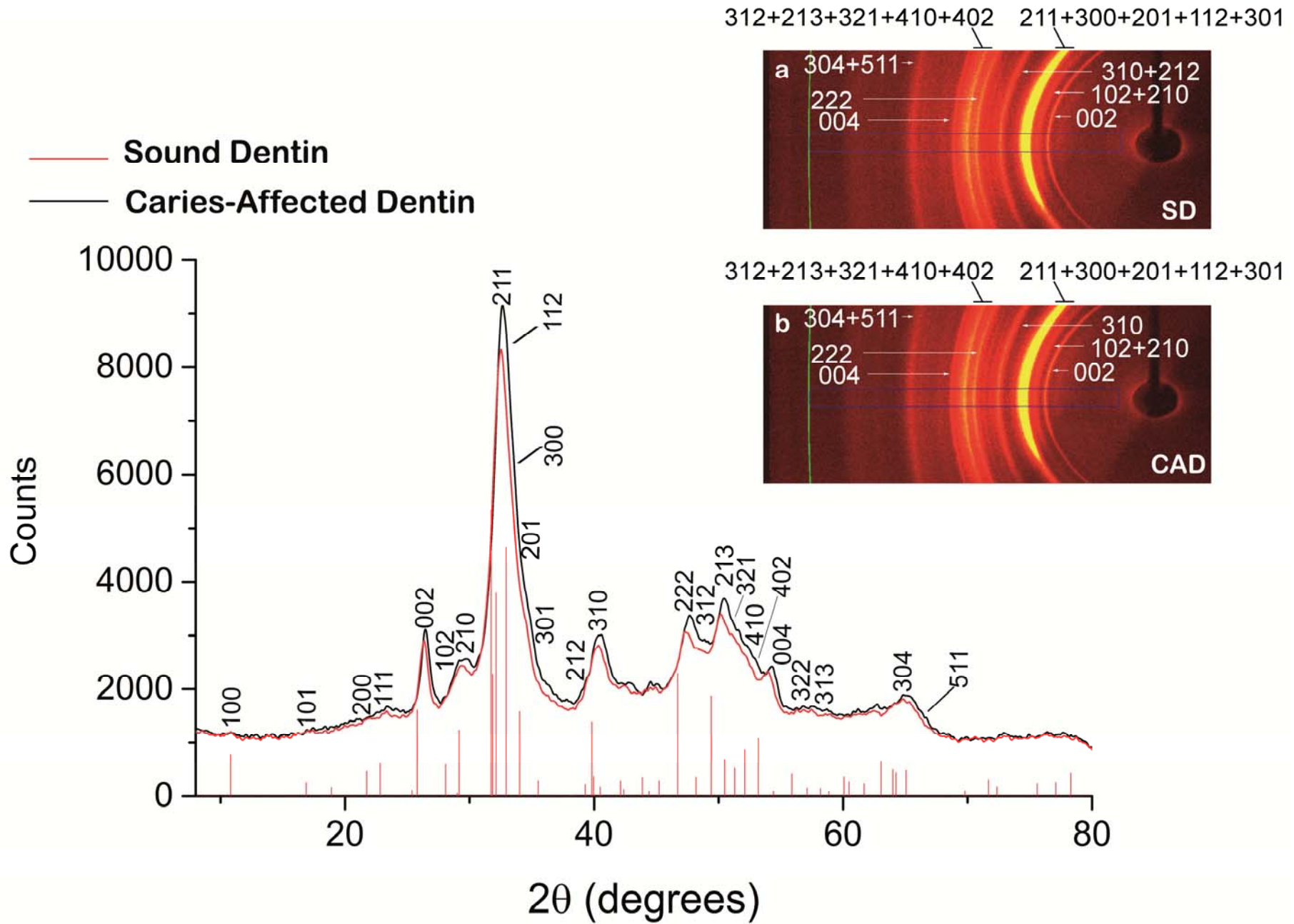


FIGURE 6

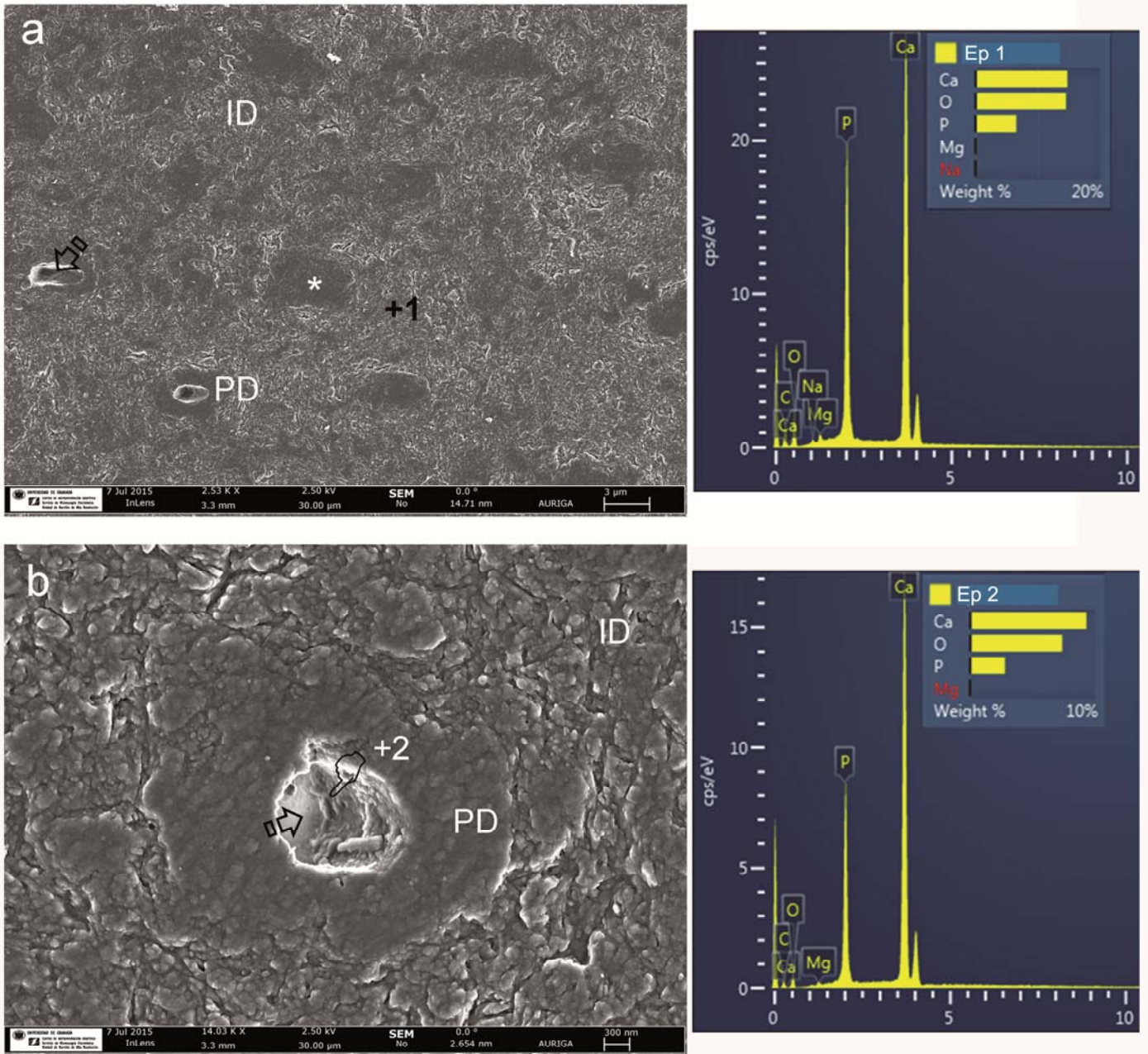


FIGURE 7

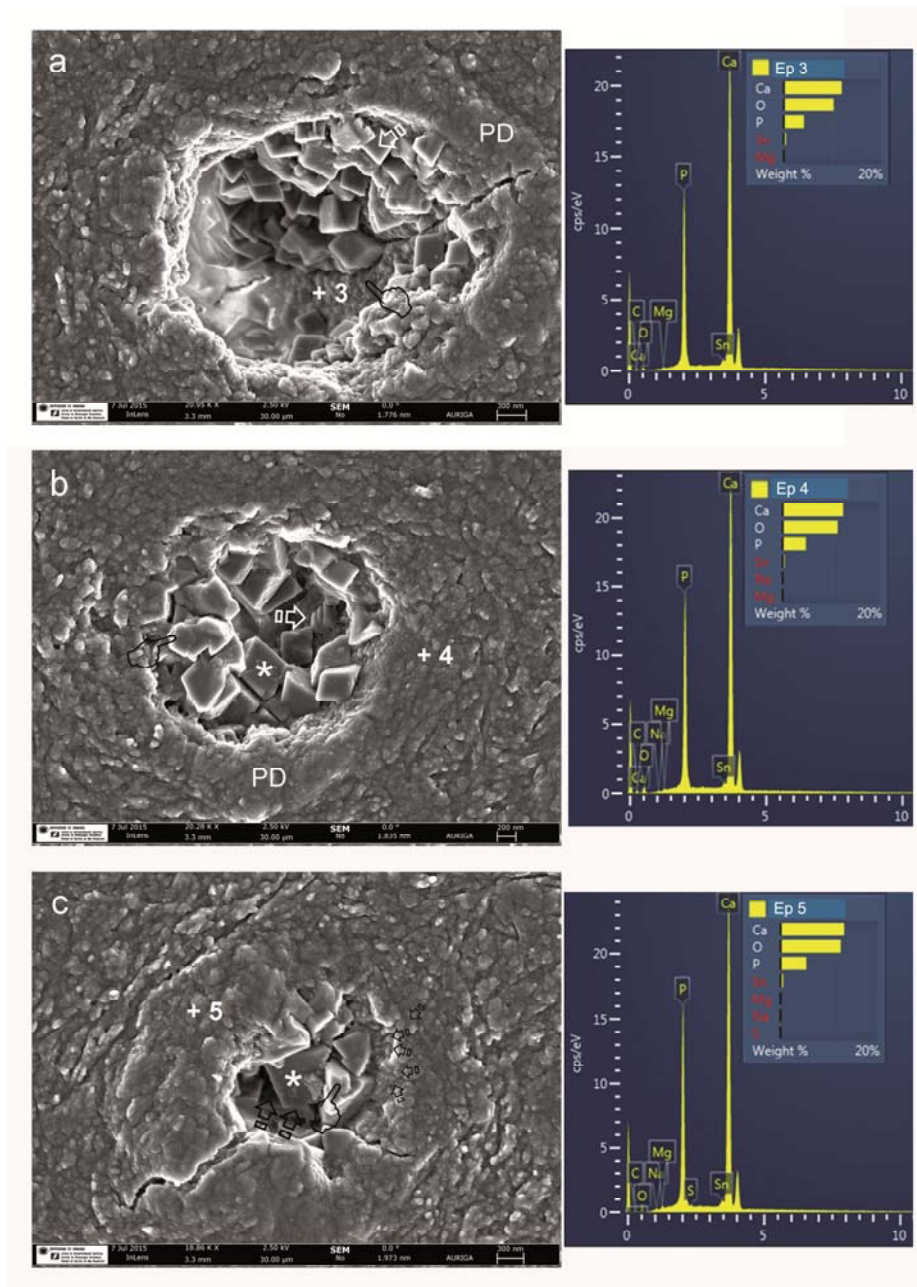


FIGURE 8

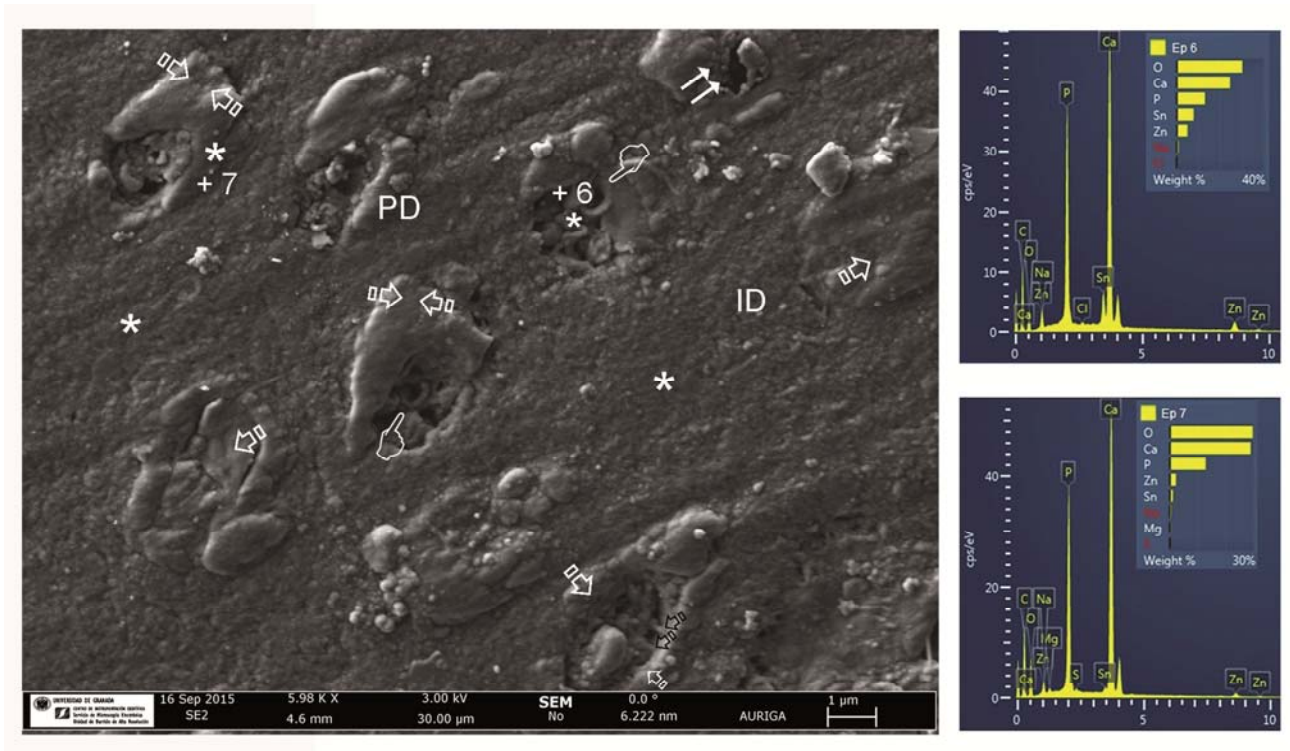
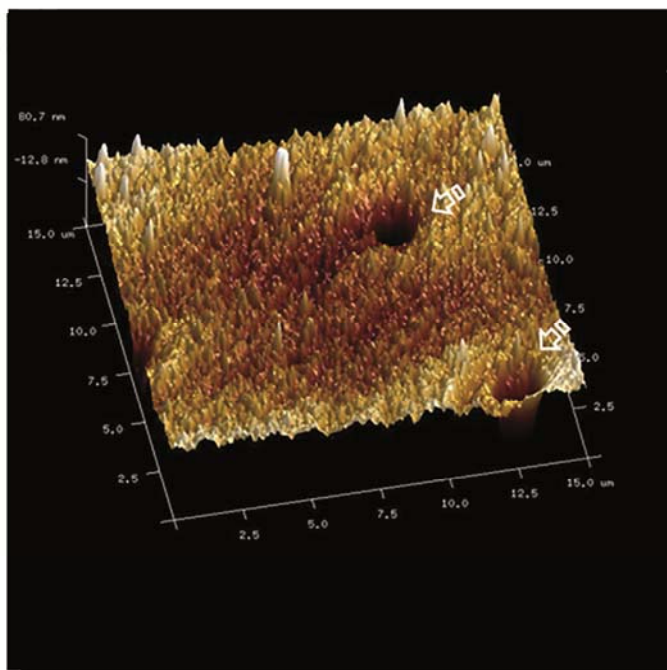


FIGURE 9 a,b

a



b

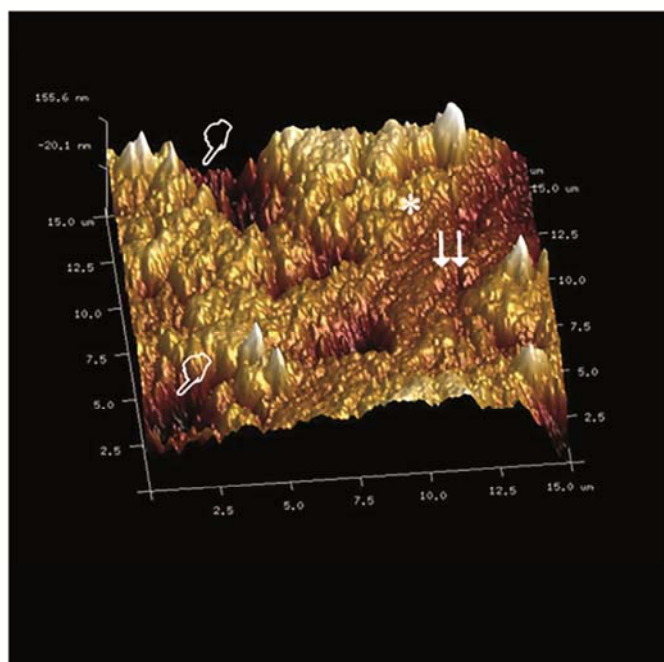
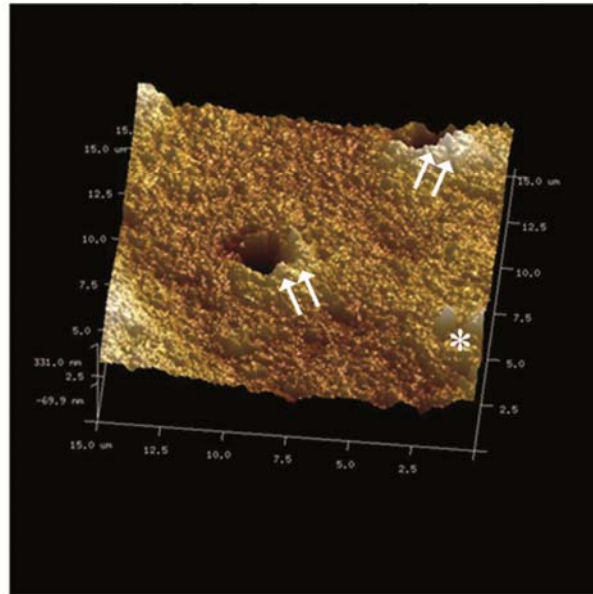


FIGURE 9 c,d

C



d

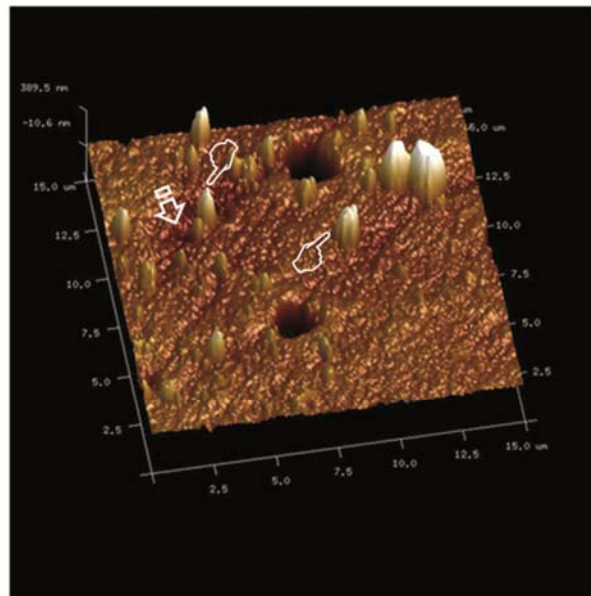
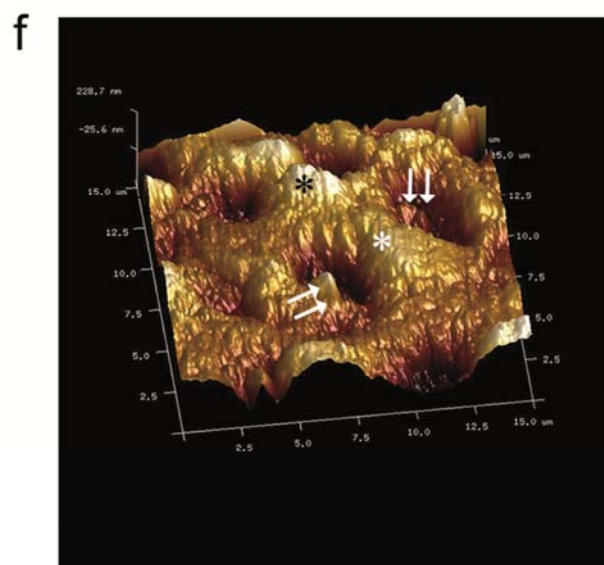
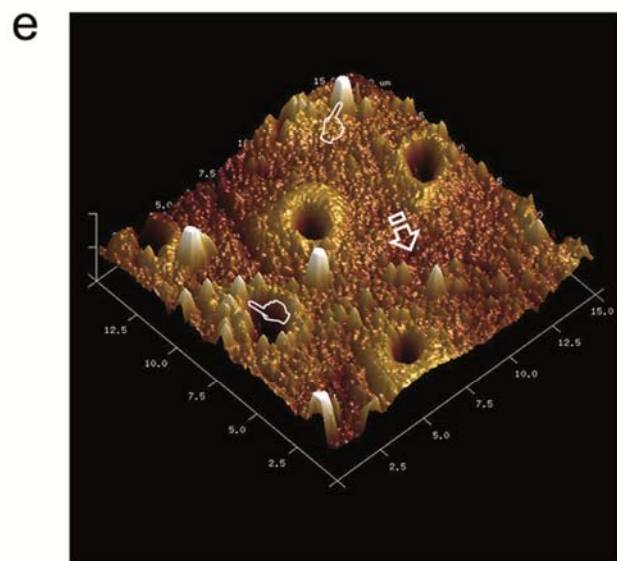


FIGURE 9 e,f



**FIGURE 10**

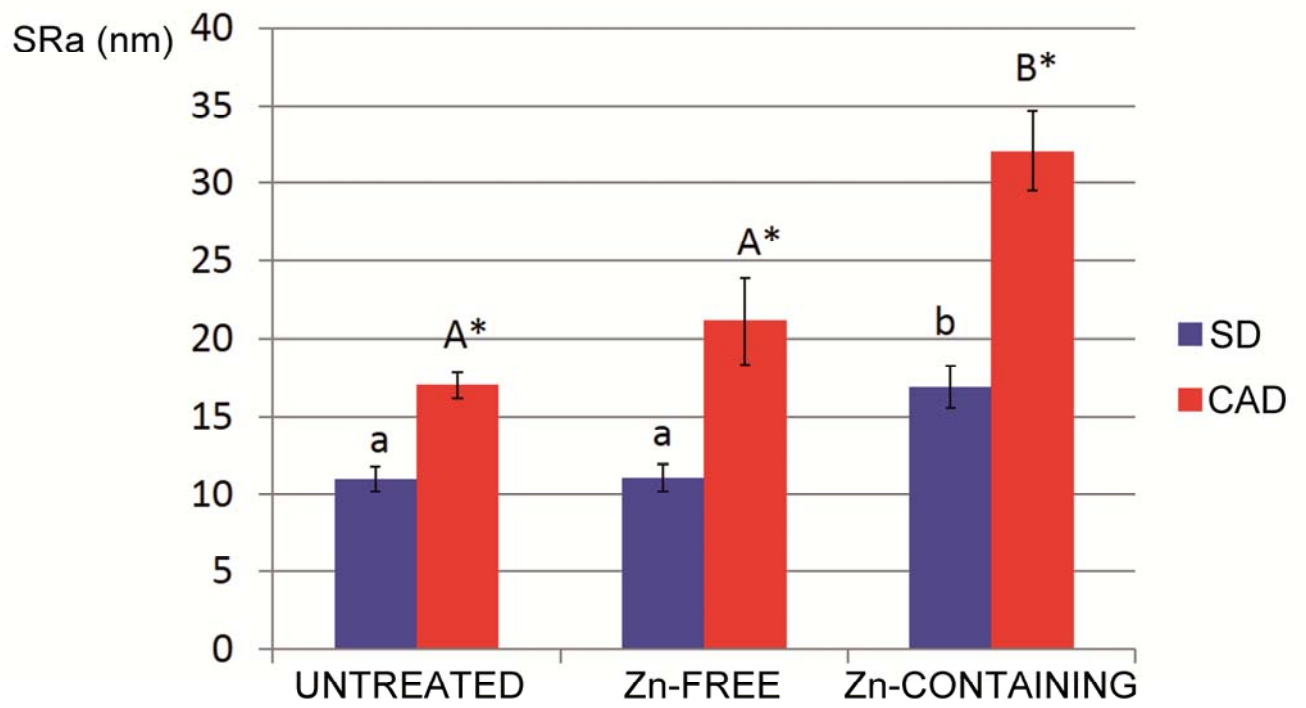


FIGURE 11

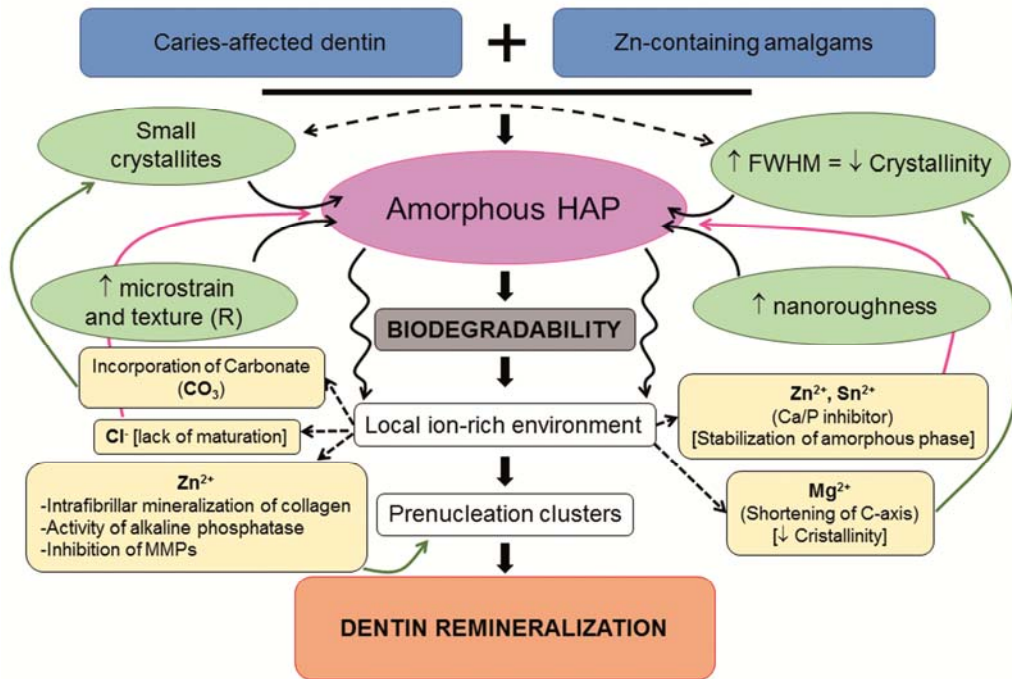


FIGURE vTOC

